

# Frequency-Enhanced Hilbert Scanning Mamba for Short-Term Arctic Sea Ice Concentration Prediction

Feng Gao, *Member, IEEE*, Zheng Gong, Wenli Liu, Yanhai Gan, Zhuoran Zheng, Junyu Dong, *Member, IEEE*, Qian Du, *Fellow, IEEE*

**Abstract**—While Mamba models offer efficient sequence modeling, vanilla versions struggle with temporal correlations and boundary details in Arctic sea ice concentration (SIC) prediction. To address these limitations, we propose Frequency-enhanced Hilbert scanning Mamba Framework (FH-Mamba) for short-term Arctic SIC prediction. Specifically, we introduce a 3D Hilbert scan mechanism that traverses the 3D spatiotemporal grid along a locality-preserving path, ensuring that adjacent indices in the flattened sequence correspond to neighboring voxels in both spatial and temporal dimensions. Additionally, we incorporate wavelet transform to amplify high-frequency details and we also design a Hybrid Shuffle Attention module to adaptively aggregate sequence and frequency features. Experiments conducted on the OSI-450a1 and AMSR2 datasets demonstrate that our FH-Mamba achieves superior prediction performance compared with state-of-the-art baselines. The results confirm the effectiveness of Hilbert scanning and frequency-aware attention in improving both temporal consistency and edge reconstruction for Arctic SIC forecasting. Our codes are publicly available at <https://github.com/oucalab/FH-Mamba>.

**Index Terms**—Arctic sea ice, Vision Mamba, Hilbert scanning, Sea ice concentration, Spatio-temporal sequence prediction

## I. INTRODUCTION

As a critical component of the global climate system, Arctic sea ice plays a fundamental role in regulating both regional and global temperatures through the albedo effect. By reflecting incoming solar radiation, it helps maintain the Earth's energy balance [1]. In recent decades, Arctic sea ice has been melting at a rate significantly faster than previously anticipated, signaling alarming shifts in climate patterns. Accurate prediction of Arctic sea ice dynamics is therefore essential for advancing our understanding of climate change and ensuring safe navigation in the Arctic. Moreover, the development of reliable forecasting models is becoming increasingly important for geopolitical planning and long-term environmental stewardship in this rapidly changing region [2].

Existing sea ice concentration (SIC) prediction methodologies can be broadly classified into two main categories: physics-driven methods [3] and data-driven methods [4], [5].

This work was supported in part by the National Science and Technology Major Project of China under Grant 2022ZD0117201, in part by the Natural Science Foundation of Shandong Province under Grant ZR2024MF020. (Corresponding author: Yanhai Gan)

Feng Gao, Zheng Gong, Chuanzheng Gong, Yanhai Gan, and Junyu Dong are with the State Key Laboratory of Physical Oceanography, Ocean University of China, Qingdao 266100, China.

Zhouran Zheng is with the School of Cyber Science and Technology, Sun Yat-Sen University, Shenzhen 518197, China.

Qian Du is with the Department of Electrical and Computer Engineering, Mississippi State University, Starkville, MS 39762 USA.

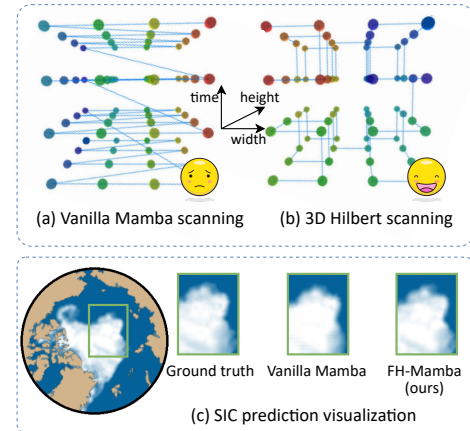


Fig. 1. Comparison of vanilla Mamba and 3D Hilbert scanning. (a) Scanning route by vanilla Mamba. (b) Scanning route by 3D Hilbert. (c) Visualization of SIC prediction. The lines and endpoints are shaded in gradients from red to green, representing the route of the scan. Vanilla Mamba struggles to effectively model temporal correlation of SIC sequences, while our FH-Mamba leverages the 3D Hilbert curve's locality characteristic to enhance the spatiotemporal learning.

Recent surveys have also provided comprehensive reviews of these data-driven spatiotemporal prediction methodologies [6], [7]. Physics-driven approaches rely on numerical models that simulate sea ice behavior by solving coupled dynamic and thermodynamic equations. These models incorporate physical laws and external forcing factors such as wind, ocean currents, and atmospheric conditions to predict sea ice changes. While they provide interpretable and physically consistent forecasts, their accuracy is often limited by model complexity, parameterization uncertainty, and high computational costs.

In contrast, data-driven approaches (particularly those based on deep learning) have shown significant improvement in Arctic SIC prediction due to their ability to automatically extract spatiotemporal features and nonlinear patterns from large volumes of observational data. Deep learning models such as IceNet [8], SICNet [9], FCNet [10], and IceDiff [11] have demonstrated effective performance in capturing the intricate relationships among multiple variables, improving prediction accuracy. These advances highlight the growing potential of deep learning in addressing the challenges of SIC forecasting in a rapidly changing Arctic environment.

Despite these successes, many deep learning architectures, particularly those based on Transformers [12], encounter computational bottlenecks when processing the extensive spatiotemporal data inherent in climate modeling. This challenge

has spurred research into alternative architectures with greater efficiency for long-sequence modeling.

Recently, State Space Models (SSMs) have shown their superiority in natural language processing [13], image restoration [14], [15], [16], and hyperspectral image processing [17], [18], [19], particularly due to their linear complexity when dealing with long sequences. By formalizing discrete state space equations recursively, Mamba can capture long-range dependencies [20], thereby improving sequence prediction quality in abrupt climatic impacts. Additionally, the linear-time complexity of Mamba in processing sequential data makes it particularly suitable for handling massive remote sensing satellite data, effectively reducing computational overhead while maintaining prediction accuracy.

However, adapting Mamba-based models to SIC prediction faces challenges due to two main limitations: (1) *It emphasizes the spatial continuous information in a single image, but struggles to effectively model temporal correlations.* It emphasizes the spatial continuous information in a single image, but struggles to effectively model spatiotemporal correlations due to the naive data processing strategy. As shown in Fig. 1(a), this baseline approach recursively processes frames that are flattened into 1D sequences. Unlike Convolutional RNNs (e.g., ConvLSTM) that preserve 2D spatial structures while iterating through time, the standard flattening process in vanilla Mamba converts the 3D spatiotemporal volume into a global 1D sequence using a fixed scanning order (e.g., raster scan). This method creates a significant theoretical gap between the 1D scanned sequence and the inherent 3D sea ice dynamics: spatially and temporally adjacent grid points in the real world become widely separated in the flattened 1D sequence. For instance, the index distance between a pixel at time  $t$  and the same pixel at time  $t + 1$  equals the total number of pixels in a frame. This disruption of spatiotemporal locality makes it difficult for the SSM to capture the local evolution patterns of sea ice changes effectively. Therefore, how to effectively model the temporal correlations among sea ice sequences poses a critical challenge. (2) *The Mamba model is prone to missing boundary details of the Arctic margin regions.* Mamba performs its attention mechanism via a scanning process, which results in the erosion of intrinsic local spatial details. For the Arctic sea ice margin, where boundary details are often subtle and scattered across the image, existing Mamba-based methods struggle to retain the critical spatial cues. Hence, how to seamlessly incorporate these spatial details while concurrently improving prediction performance is a pivotal challenge.

To address these limitations, as shown in Fig. 2, we propose the **Frequency-Enhanced Hilbert Scanning Mamba** framework (**FH-Mamba**), which aims to fully exploit the temporal and local features for short-term Arctic sea ice prediction. Firstly, to mitigate the limitation of temporal correlation, we introduce *3D Hilbert scan mechanism* that capitalizes on the inherent locality of the Hilbert curve to enhance the spatiotemporal learning capabilities of the vanilla Mamba. The differences between vanilla Mamba and 3D Hilbert scanning are depicted in Fig. 1. The scanning is performed across both temporal and spatial dimensions, enhancing the model's

ability to capture temporal-level local information. Secondly, to address the loss of spatial detail in marginal regions, we use wavelet transform to enhance the high-frequency details. To further capture the complex dependencies across the sequence and frequency features, we design *Hybrid Shuffle Attention (HSA)* module to aggregate the sequence and frequency features by calculating attentions within corresponding channels. As illustrated in Fig. 1(c), this design effectively leverages the complementary information between sequence and frequency domains, leading to improved spatial detail preservation in marginal regions.

Our main contributions can be summarized as follows:

- We propose FH-Mamba, a novel framework that employs 3D Hilbert scanning mechanism for Arctic SIC prediction. The scanning is performed across both temporal and spatial dimensions, enhancing the model's capability to capture temporal-level local information.
- We employ wavelet transform to enhance high-frequency details in the margin regions. Additionally, we design a Hybrid Shuffle Attention (HSA) module to fuse sequence and frequency features, effectively exploiting their complementary information.
- We conduct extensive experiments on two benchmark datasets demonstrating that our FH-Mamba outperforms state-of-the-art methods. To support the Arctic and climate research community, we will release the code publicly.

## II. RELATED WORKS

### A. Deep Learning-based Sea Ice Prediction

Deep learning has made remarkable strides in Arctic sea ice concentration (SIC) prediction by leveraging deep neural networks to model the complex, nonlinear relationships inherent in observational data. For instance, ConvLSTM is employed to model the spatio-temporal correlations for SIC prediction [21], demonstrating superiority over traditional autoregressive models. To better incorporate spatial context, subsequent works utilized architectures like Convolutional Neural Networks (CNNs) [22] and Transformer [23] for weekly SIC prediction. More recently, U-Net [24] based models have become prominent, such as SICNet [9] and FCNet [10] for short-term forecasts. IceDiff [11] combines Swin Transformer [25] with a diffusion model in a two-stage framework for Arctic SIC prediction and super-resolution. Recently, IceMamba [26] employs SSMs for Pan-Arctic sea ice prediction.

Despite their effectiveness, Mamba-based SIC prediction methods do not fully exploit the temporal correlations among SIC frames. In this paper, we employ a 3D Hilbert mechanism to enhance the temporal learning capabilities. Employing the 3D Hilbert mechanism enhances temporal learning by preserving spatial and temporal locality, enabling the model to better capture sequential dependencies and fine-grained spatiotemporal patterns in Arctic data.

### B. State Space Models for Vision Task

SSMs, particularly Mamba-based architectures, are being actively adapted for computer vision tasks, leveraging their

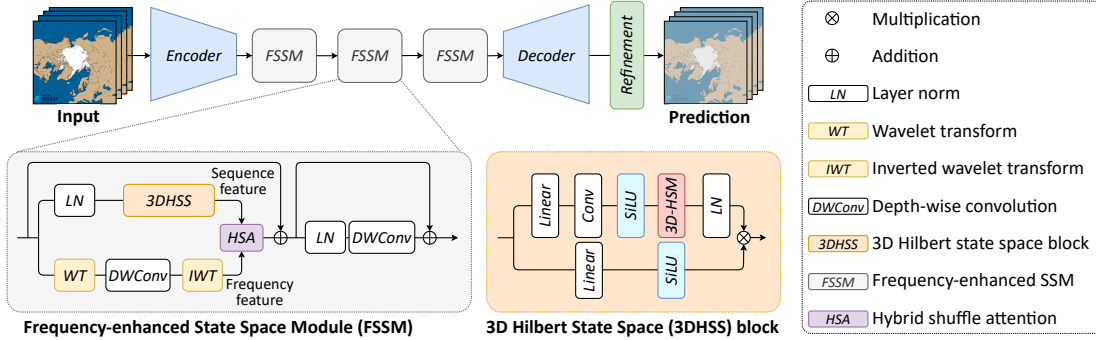


Fig. 2. Framework of our Frequency-Enhanced Hilbert scanning Mamba (FH-Mamba) for short-term Arctic sea ice concentration prediction. It is composed of a feature encoder, a series of Frequency-enhanced State Space Module (FSSM), and a feature decoder. The FSSM employs the 3D Hilbert State Space (3DHSS) block and wavelet transform to capture spatio-temporal feature dependencies. In 3DHSS, we use 3D Hilbert scanning mechanism to capture temporal-level local information. Furthermore, Hybrid Shuffle Attention (HSA) module is designed to fuse sequence and frequency features, effectively exploiting their complementary information.

efficiency in modeling long-range dependencies beyond 1D sequences. To better handle 2D spatial information, Def-Mamba [27] introduces deformable mamba blocks that dynamically adjust the scanning path to focus on salient image features. GroupMamba [28] addresses scaling challenges by proposing modulated group Mamba layer, which processes channel groups with independent, multi-directional scanning to improve stability and performance. Hybrid approaches have also emerged, such as MambaVision [29], which integrates self-attention blocks into the final layers of a Mamba backbone to enhance its capacity for capturing long-range spatial relationships. For deployment on resource-constrained devices, EfficientViM [30] presents an architecture that reduces computational cost by performing channel mixing within compressed hidden states. To enhance the temporal feature learning, RainMamba [31] uses Hilbert scanning to exploit sequence correlations in videos for deraining task.

Unlike previous works, we employ wavelet transform to enhance fine-grained details in the Arctic margin regions. Furthermore, we design a HSA module to effectively exploit the complementary information between sequence and frequency features. This enables the model to capture more comprehensive spatiotemporal dependencies and improves prediction accuracy.

### III. METHODOLOGY

#### A. Problem Statement

We address the task of short-term Arctic sea ice concentration (SIC) prediction, which aims to forecast future daily SIC maps based on a sequence of past observations. Specifically, given the SIC data from the past  $L_i$  days, represented as a sequence  $\mathbf{X} = \{x_l\}_{l=1}^{L_i} \in \mathbb{R}^{L_i \times C \times H \times W}$ , where  $L_i$  denotes the input sequence length, the goal is to model the conditional distribution  $p(\mathbf{Y}|\mathbf{X})$  of the next  $L_o$  frames, denoted as  $\mathbf{Y} = \{y_l\}_{l=1}^{L_o} \in \mathbb{R}^{L_o \times C \times H \times W}$ , where  $L_o$  represents the output prediction length. Here  $H$  and  $W$  refer to the spatial resolution (height and width) of each SIC frame, and  $C = 1$  indicates that only the SIC variable is used in the prediction. This formulation treats sea ice prediction as a spatiotemporal sequence forecasting problem, where the model must learn to

capture both spatial structures and temporal dynamics in the evolving sea ice field. Accurately modeling  $p(\mathbf{Y}|\mathbf{X})$  is critical for anticipating short-term Arctic sea ice behavior.

#### B. Overall Framework

The proposed FH-Mamba framework is shown Fig. 2, which is composed of a feature encoder, a series of Frequency-enhanced State Space Module (FSSM), and a feature decoder. The encoder contains several convolutional blocks, each consisting of two-dimensional (2D) convolution, layer normalization, and LeakyReLU activation, to extract spatial features. The obtained spatial features are successively fed into FSSM for spatial and temporal feature exploitation. After that, a decoder containing several transposed convolutional blocks, which include 2D transposed convolution, group normalization, and LeakyReLU activation, is employed to reconstruct the ground truth frames. It should be noted that two depth-wise convolution layers are employed as the refinement block to optimize the spatial details of the SIC prediction results.

The FSSM is the critical component in our FH-Mamba, and details of the module are shown in Fig. 2. The input features are fed into two branches, namely Mamba and frequency branches. The Mamba branch uses 3D Hilbert State Space (3DHSS) block to exploit the spatial-temporal features. The frequency branch employs wavelet to enhance the high-frequency details. The output of both branches are fused via Hybrid Shuffle Attention (HSA). Afterwards, a depth-wise convolution layer is employed for non-linear feature transformation. Next, we introduce the 3D Hilbert scanning mechanism in Section III. C, elaborate the 3DHSS block in Section III. D, and present the Hybrid Shuffle Attention in Section III. E. The overall optimization objective is summarized in Section III. F.

#### C. 3D Hilbert Scanning Mechanism

The Hilbert curve is a continuous space-filling curve that maps a one-dimensional interval onto a multi-dimensional space while preserving locality [32]. Originally proposed by David Hilbert [33], the curve has found extensive use in computer graphics [34], spatial indexing [35], and deep learning

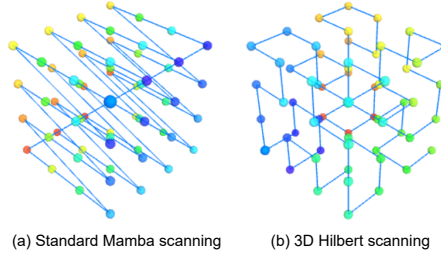


Fig. 3. Trajectories of standard Mamba and 3D Hilbert scanning.

[36] due to its ability to maintain spatial proximity between neighboring points.

**3D Hilbert Curve.** Let  $H : [0, 1] \rightarrow [0, 1]^d$  be a  $d$ -dimensional Hilbert curve of order  $n$ , where  $d$  is the spatial dimensionality and  $n$  controls the resolution. In discrete form, a Hilbert curve of order  $n$  in  $d$  dimensions maps a scalar index  $i \in \{0, 1, \dots, 2^{dn} - 1\}$  to a coordinate  $H(i) \in \{0, 1, \dots, 2^n - 1\}^d$ . The mapping ensures that consecutive indices correspond to spatially adjacent or nearby points, thereby preserving locality [37], [38]. In the context of 3D data (the Arctic sea ice concentration spatio-temporal volumes), the 3D Hilbert curve extends the locality-preserving property into three-dimensional space [39]. It defines a traversal path through a 3D cube of size  $2^n \times 2^n \times 2^n$ , such that adjacent indices in the one-dimensional sequence correspond to neighboring voxels in the 3D grid. This is particularly valuable in SSMs benefits from spatial or temporal coherence. Let  $V \in \mathbb{R}^{T \times C \times H \times W}$  be a 3D spatio-temporal volume, where  $T$  is the temporal length,  $C$  is the number of channels, and  $H \times W$  is the spatial resolution. The 3D Hilbert scanning function  $\phi : \mathbb{Z}^4 \rightarrow \mathbb{Z}$  maps each voxel at position  $(t, c, h, w)$  to a unique index  $i$  along the Hilbert curve, producing a flattened sequence  $\{v_i\}_{i=1}^N$ , where  $N = T \cdot C \cdot H \cdot W$ . This scan preserves the spatial and temporal proximity, allowing for effective modeling of localized correlations in the Arctic Sea Ice Concentration (SIC) data sequence. In this paper, we use the Generalized Hilbert algorithm for space filling for 3D data. The idea is to recursively apply the following template to obtain a Hilbert-like curve. A general rectangle with a known orientation is split into three regions (“up”, “right”, “down”), for which the function calls itself recursively, until a trivial path can be produced [40].

**Comparisons of 3D Hilbert Scanning and Standard Mamba Scanning.** Standard Mamba scanning typically flattens the spatio-temporal input data into a 1D sequence in a linear order. This flattening disrupts the intrinsic spatial and temporal adjacency, leading to a loss of structural information crucial for capturing ice dynamics. However, 3D Hilbert scanning preserves local neighborhood continuity in both spatial and temporal dimensions, maintaining the inherent topology of Arctic sea ice evolution. For prediction accuracy, standard Mamba scanning suffers from limited spatial detail reconstruction, especially in marginal ice zones where precise prediction is crucial. At the same time, 3D Hilbert Scanning improves spatial detail preservation by enhancing the sequence’s locality, leading to better reconstruction of complex sea ice patterns and reduced prediction bias in marginal areas.

Fig. 3 illustrates the difference between Standard Mamba scanning and 3D Hilbert scanning in terms of their traversal paths through a 3D spatiotemporal volume. Standard Mamba scanning visits points along a fixed direction (e.g., time-major or spatial-major order). This approach does not preserve the spatial or temporal locality; neighboring points in 3D space may be far apart in the flattened sequence. However, 3D Hilbert scanning traverses the 3D volume in a way that maintains local continuity. The scanning path visits neighboring points in a spatially and temporally coherent order, preserving locality and structural integrity of the input data. It is evident that 3D Hilbert scanning (right) provides a more topology-aware and locality-preserving trajectory compared to the standard Mamba scanning strategy (left), which is essential for modeling complex spatial-temporal patterns in Arctic sea ice prediction.

**Hilbert Scanning vs. Graph Approaches.** It is worth noting that while 3D Hilbert scanning preserves locality better than raster scanning, it still faces the boundary problem, where spatially adjacent voxels may be distant in the flattened 1D sequence. Graph Neural Networks (GNNs) could theoretically solve this by explicitly modeling adjacency via edges. However, for dense regular grid data like sea ice data, GNNs often incur prohibitive computational costs due to the massive number of nodes and edges required for fine-grained prediction. In contrast, our Mamba-based approach maintains linear complexity. Furthermore, the limitation of the Hilbert curve is effectively mitigated in FH-Mamba by two factors: First, the SSM’s inherent ability to model long-range dependencies allows it to connect distant elements in the sequence. Second, the CNN-based encoder and the parallel Wavelet branch capture 2D spatial structures and high-frequency boundaries independently of the scanning order, ensuring that local adjacency information is not lost due to sequence discontinuity.

#### D. 3D Hilbert State Space Block

**Mamba Block.** For the Mamba block, we adopt a structure similar to that of Vision Mamba [41]. As shown in Fig. 2, it consists of LayerNorm (LN), Linear layers, 1D Convolution, and 3D Hilbert SSM. Given an input  $\mathbf{X} \in \mathbb{R}^{B \times L \times D}$ , where  $B$ ,  $L$ , and  $D$  denote the batch size, the length of 1D data, and the feature dimension, respectively. The output  $\mathbf{X}'$  is computed as:

$$\mathbf{X}'_1 = \text{LN}(\mathbf{X}), \quad (1)$$

$$\mathbf{X}'_2 = \text{3D\_Hilbert\_SSM}(\text{Silu}(\text{Conv}(\text{Linear}(\mathbf{V}'_1)))), \quad (2)$$

$$\mathbf{V}' = \text{Linear}(\mathbf{V}'_2 \odot \text{Silu}(\text{Linear}(\mathbf{V}'_1))), \quad (3)$$

where  $\odot$  denotes the element-wise multiplication. It is worth noting that we use a 3D Hilbert scan instead of the original global scan in Vision Mamba. Both forward and backward scans are employed in our implementation.

#### E. Hybrid Shuffle Attention

Hybrid Shuffle Attention (HSA) aggregates the 3D Hilbert sequence and frequency features by calculating attentions

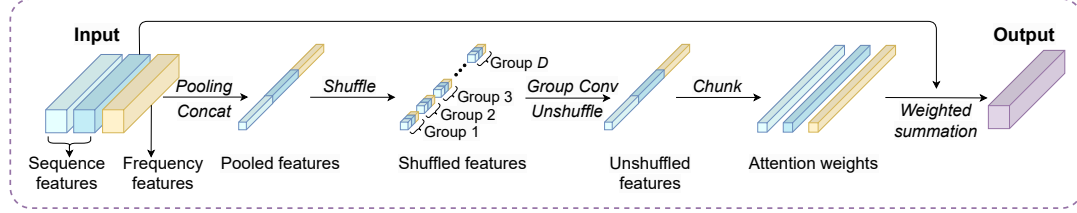


Fig. 4. Illustration of the Hybrid Shuffle Attention (HSA). The input sequence and frequency features  $\{x^1, x^2, x^f\}$  are handled by pooling and concatenation to generate  $\hat{\mathbf{X}}$ . It undergoes the shuffle operation and results in  $\hat{\mathbf{X}}'$ . Afterwards,  $\hat{\mathbf{X}}'$  are split into  $D$  groups. Group convolution and unshuffle operation are employed, generating unshuffled weights  $\hat{\mathbf{A}}$ . The weights are further chunked and reshaped into attention weights  $\{\mathbf{A}^1, \mathbf{A}^2, \mathbf{A}^f\}$ . Finally, the output is computed by performing weighted summation of the input features and the attention weights.

within corresponding channels. This design enables it to capture complex dependencies across distinct sequences, thus better leveraging complementary information from different scanning directions. As shown in Fig. 4, supposing two sequence features  $x^1$  and  $x^2$ , and frequency features  $x^f$ , we first apply the spatial average pooling to reduce the computational cost, and then concatenate as:

$$\begin{aligned}\hat{\mathbf{X}} &= \text{concat}(\text{GAP}(x^1, x^2, x^f)) \\ &= [x_1^1, \dots, x_D^1, x_1^2, \dots, x_D^2, x_1^f, \dots, x_D^f],\end{aligned}\quad (4)$$

where  $x_d^k$  is the pooled feature in  $d$ -th channel of  $k$ -th sequence, and  $x_d^f$  is the pooled feature in  $d$ -th channel of the frequency feature.  $D$  is the feature dimension. Afterwards, we employ sequence shuffle operation to rearrange feature as follows:

$$\begin{aligned}\hat{\mathbf{X}}' &= \text{shuffle}(\hat{\mathbf{X}}) \\ &= [x_1^1, x_1^2, x_1^f, x_2^1, x_2^2, x_2^f, \dots, x_D^1, x_D^2, x_D^f].\end{aligned}\quad (5)$$

Afterwards, we employ group convolution with group size three to obtain the channel-wise attention weights and unshuffle the weights back to the original order as follows:

$$\begin{aligned}\hat{\mathbf{A}} &= \text{unshuffle}(\text{GConv}(\hat{\mathbf{X}}')) \\ &= [w_1^1, \dots, w_D^1, w_1^2, \dots, w_D^2, w_1^f, \dots, w_D^f],\end{aligned}\quad (6)$$

where  $\text{GConv}(\cdot)$  is the group convolution. The unshuffled weights  $\hat{\mathbf{A}}$  are chunked as  $\{\mathbf{A}^1, \mathbf{A}^2, \mathbf{A}^f\} = \text{chunk}(\hat{\mathbf{A}})$ , where  $\text{chunk}(\cdot)$  is the chunk operation. Finally, weight summation is used to generate the output, which can be formulated as:

$$\mathbf{Y} = \mathbf{A}^1 \mathbf{x}^1 + \mathbf{A}^2 \mathbf{x}^2 + \mathbf{A}^f \mathbf{x}^f, \quad (7)$$

and  $\mathbf{Y}$  is the output of HSA.

#### F. Loss Function

To ensure that the predicted SIC sequences aligns with the ground truth at the pixel level, we use L1 loss to measure the discrepancy between the final prediction  $\hat{\mathbf{Y}}$  and the ground truth target  $\mathbf{Y}$ :

$$\mathcal{L}_{rec} = \|\hat{\mathbf{Y}} - \mathbf{Y}\|_1. \quad (8)$$

We also use the gradient loss to preserve edges and fine details by comparing gradients:

$$\mathcal{L}_{grad} = \|\nabla \hat{\mathbf{Y}} - \nabla \mathbf{Y}\|_1, \quad (9)$$

where  $\nabla$  denotes the gradient operator. The final total loss is a weighted summation of both loss terms:

$$\mathcal{L}_{total} = \mathcal{L}_{rec} + \lambda \mathcal{L}_{grad}, \quad (10)$$

where  $\lambda$  is a hyperparameter that balances the reconstruction and detail preservation.

## IV. EXPERIMENTAL RESULTS AND ANALYSIS

### A. Datasets

We evaluate our proposed FH-Mamba model for Sea Ice Concentration (SIC) prediction using the OSI-450a1 dataset. As an updated version of the OSI-450a1 dataset [42], OSI-450a1 is sourced from the OSI-SAF website and represents a full reprocessing of SIC data from 1978 to 2020 with optimized data processing. It includes coarse-resolution images ( $432 \times 432$  pixels) from SMMR (1978–1987), SSM/I (1987–2008), and SSMIS (2006–2020) satellites, along with ECMWF ERA-Interim data [43]. Model assessments are performed within the Arctic Monitoring and Assessment Program (AMAP) region [44], north of the Arctic Circle, to demonstrate the significance of SIC prediction for understanding the sea ice system's impact on environmental and human activities. We utilize data spanning from October 25, 1978, to December 31, 2020, dividing it into a training set (1978–2010), a validation set (2011–2015), and a test set (2016–2020), containing 11,729, 1,799, and 1,800 samples, respectively.

To further evaluate the generalization capability of our model, especially on data with different sensor characteristics and significantly higher spatial resolution, we also conduct experiments on the AMSR2 Sea Ice Concentration (SIC) dataset [45]. This dataset is provided by the University of Bremen, sourced from the AMSR2 sensor aboard the Japan Aerospace Exploration Agency (JAXA)'s GCOM-W1 satellite. It offers daily sea ice concentration data from July 2012 to the present with a spatial resolution of 3.125 km, which is substantially finer than the 25 km resolution of the OSI-450a1 dataset. We employed the Spatio-Temporal Inverse Distance Weighting algorithm with a Gaussian kernel to interpolate the missing data points in AMSR2 data. Subsequently, pixels with more than 95% missing data throughout the time series were identified as land and excluded from the analysis. For the AMSR2 dataset, we use the data from August 12, 2012, to December 31, 2023, serving as the training set. Data from January 1, 2024, to December 31, 2024, are employed as the

TABLE I

PREDICTION PERFORMANCE OF DIFFERENT METHODS ON THE OSI-450-a1 DATASET. THE **BOLD** AND UNDERLINE DENOTE THE BEST AND SECOND RESULTS. (NSE VALUES ADJUSTED FOR CONSISTENCY WITH RMSE)

Method	RMSE (%) ↓						MAE (%) ↓						NSE (%) ↑					
	2016	2017	2018	2019	2020	2016	2017	2018	2019	2020	2016	2017	2018	2019	2020	2016	2017	2018
ConvLSTM	9.148	8.466	8.838	8.738	9.093	2.967	2.733	2.755	2.749	2.855	92.597	94.537	94.223	94.083	93.069			
PredRNN	9.054	8.356	8.505	8.360	8.827	2.938	2.679	2.642	2.635	2.777	92.691	94.729	94.636	94.674	93.431			
PredRNNv2	8.807	8.219	8.526	8.362	8.649	2.852	2.665	2.671	2.673	2.750	93.196	94.967	94.746	94.753	93.844			
IceNet	9.511	8.636	9.088	8.803	9.128	3.064	2.715	2.827	2.714	2.819	91.878	94.207	93.546	93.939	92.577			
SimVP	7.472	6.862	7.089	6.720	7.091	2.408	2.308	2.210	2.095	2.233	95.296	96.578	96.331	96.698	95.870			
SwinLSTM	7.258	6.769	6.784	6.739	6.881	2.341	2.211	2.160	2.167	2.176	95.508	96.652	96.643	96.501	96.107			
VMRNN	7.224	6.901	7.089	6.901	7.101	2.418	2.268	2.282	2.207	2.285	95.683	96.462	96.276	96.429	95.975			
FCNet	7.276	6.751	6.884	6.958	6.897	2.327	2.131	2.193	2.128	2.168	95.671	96.573	96.543	96.691	96.099			
IceMamba	7.135	6.676	6.850	6.735	6.885	2.424	2.258	2.230	2.195	2.243	95.745	96.734	96.577	96.538	96.105			
<b>FH-Mamba (Ours)</b>	<b>7.069</b>	<b>6.606</b>	<b>6.777</b>	<b>6.602</b>	<b>6.798</b>	<b>2.211</b>	<b>2.051</b>	<b>2.049</b>	<b>1.994</b>	<b>2.074</b>	<b>95.849</b>	<b>96.825</b>	<b>96.650</b>	<b>96.767</b>	<b>96.152</b>			

validation set and data from January 1, 2025, to August 31, 2025, are employed as the test set, containing 4,102, 339, and 188 samples, respectively.

### B. Experimental Setup

To ensure temporal continuity and data consistency, we performed specific preprocessing prior to input generation. Since the OSI-450a1 dataset is a reprocessed product without spatial gaps (e.g., pole holes), we focused on filling missing dates using the mean of the preceding and succeeding valid frames. Additionally, all land pixels were initialized to zero. Input/output samples are generated using a 14-day sliding window over the SIC time series. Specifically, the SIC data from the past 14 days are used to predict the SIC data for the following 14 days. FH-Mamba is trained using the AdamW optimizer with an initial learning rate of 0.001 and a batch size of 4. Model performance is quantified using Root Mean Square Error (RMSE), Mean Absolute Error (MAE), and Nash-Sutcliffe Efficiency (NSE). For RMSE and MAE, lower values indicate better prediction performance, while for NSE, values closer to 1 reflect better model performance. The experiments were conducted on hardware with an AMD EPYC 9754 CPU and a GeForce RTX 4090 GPU. Additionally, an early stopping mechanism is employed to prevent overfitting: the training process is terminated if the MAE value on the validation set fails to improve for 10 consecutive epochs.

To ensure a fair and direct comparison, all baseline results reported in this study were obtained by retraining the models using their official source code on our OSI-450a1 and AMSR2 dataset. We maintained a consistent experimental setup across all models, including identical data splits, batch sizes, and learning rates. However, to allow each baseline to achieve its optimal performance as intended by its authors, we adopted the specific loss functions and optimizers proposed in their respective original publications. This approach prevents potential performance degradation that could arise from using non-native optimization schemes and ensures that our comparison is against each model's best possible capability within our experimental framework.

TABLE II  
STATISTICAL SIGNIFICANCE ANALYSIS (PAIRED T-TEST) OF RMSE RESULTS BETWEEN FH-MAMBA AND BASELINE MODELS (2016–2020).

Comparison	t-statistic	p-value	Significance
FH-Mamba vs. SimVP	5.9557	0.0040	** ( $p < 0.01$ )
FH-Mamba vs. SwinLSTM	3.5780	0.0232	* ( $p < 0.05$ )
FH-Mamba vs. VMRNN	9.2211	0.0008	*** ( $p < 0.001$ )
FH-Mamba vs. FCNet	3.8632	0.0181	* ( $p < 0.05$ )

TABLE III  
PERFORMANCE COMPARISON OF DIFFERENT METHODS ON THE AMSR2 DATASET. THE **BOLD** AND UNDERLINE DENOTE THE BEST AND SECOND RESULTS.

Model	MAE (%) ↓	RMSE (%) ↓	NSE (%) ↑
ConvLSTM	3.75	14.32	88.02
PredRNN	3.65	14.02	88.59
PredRNNv2	3.50	13.51	89.09
IceNet	3.84	14.96	87.75
SimVP	2.89	10.85	91.58
SwinLSTM	2.74	10.58	91.69
VMRNN	2.65	10.16	91.91
FCNet	2.63	10.21	91.89
IceMamba	2.69	10.42	91.81
<b>FH-Mamba (Ours)</b>	<b>2.54</b>	<b>10.05</b>	<b>92.04</b>

### C. Comparison with State-of-the-Art Methods

We compare FH-Mamba with 8 state-of-the-art (SOTA) methods: ConvLSTM [21], PredRNN [46], PredRNNv2 [47], IceNet [8], SimVP [48], SwinLSTM [49], VMRNN [50], FCNet [10] and IceMamba [26]. ConvLSTM [21] extends standard LSTMs by replacing full connections with convolutional structures, enabling effective modeling of spatiotemporal dependencies for data sequences. PredRNN [46] introduces a recurrent memory architecture that flows both along temporal and spatial dimensions. PredRNNv2 [47] improves PredRNN with a decoupled spatiotemporal memory mechanism and a gradient highway unit, enabling deeper temporal propagation and more accurate sequence generation. IceNet [8] combines convolutional encoders with autoregressive temporal modeling to predict Arctic SIC at grid level with uncertainty estimation. SimVP [48] is a simple yet effective prediction framework that decouples spatial encoding from temporal dynamics. It employs convolutional networks for spatial representation and

lightweight temporal blocks for efficient sequence forecasting. SwinLSTM [49] integrates Swin Transformer blocks into an LSTM framework, leveraging hierarchical attention and shifted windows to capture long-range spatial dependencies in spatio-temporal data. VMRNN [50] introduces adaptive memory update mechanisms that dynamically adjust the receptive field over time, improving the model's flexibility for complex temporal patterns. FCNet [10] enhances Arctic SIC prediction by integrating adaptive frequency filtering and convolutional feature extraction to jointly capture fine-grained edges and long-term spatiotemporal variations. IceMamba [26] is a state-space-based framework for seasonal Pan-Arctic sea ice forecasting. It employs Residual Selective State Space Blocks (RESSB) to capture complex spatiotemporal dependencies while maintaining linear computational complexity for long-sequence climate data.

**Results on the OSI-450-a1 dataset.** Table I presents the prediction performance of various methods on the OSI-450-a1 dataset from 2016 to 2020. Overall, our FH-Mamba achieves the best performance in all cases. Specifically, FH-Mamba attains the lowest RMSE values (6.60 %–7.07 %) and MAE values (1.99 %–2.21 %), significantly outperforming classical recurrent networks such as ConvLSTM, PredRNN, and PredRNNv2, as well as recent Transformer-based or frequency-based models including SwinLSTM, VMRNN, and FCNet. Meanwhile, FH-Mamba consistently yields the highest NSE scores, indicating improved consistency in reproducing sea-ice dynamics. These results demonstrate that FH-Mamba effectively captures both short-term variations and long-range dependencies in Arctic sea-ice evolution, delivering more accurate and robust spatiotemporal forecasts than existing deep learning baselines. Furthermore, to evaluate whether the performance gain is statistically significant, we conduct a paired t-test based on the annual RMSE values from 2016 to 2020, as summarized in Table II. All p-values are smaller than 0.05, with the comparison against VMRNN even reaching  $p < 0.001$ . This indicates that the effective of FH-Mamba is statistically significant and robust, rather than being a result of random chance.

**Results on the AMSR2 dataset.** Table III presents the performance comparison of various spatiotemporal prediction models on the AMSR2 dataset. Among all competitors, the proposed FH-Mamba achieves the best overall performance, obtaining the lowest MAE (2.54 %) and RMSE (10.05 %), as well as the highest NSE (92.04 %). Compared with classical recurrent models such as ConvLSTM, PredRNN, and PredRNN-v2, FH-Mamba significantly reduces prediction errors and enhances numerical stability. It also surpasses advanced transformer- and frequency-based baselines (SwinLSTM, VMRNN, FCNet), demonstrating its capability to capture both local spatial structures and long-range temporal dependencies. These results verify the generalization capability of FH-Mamba across datasets, showing that the model effectively adapts to different input distributions and achieves accurate and robust Arctic sea ice forecasting.

#### D. Visual and Qualitative Analysis

**Visualization of Prediction.** In September 2020, Arctic sea ice reached a record-low minimum extent, marking one of the most significant observations. This period reflects extreme Arctic sea ice loss driven by persistent warm conditions, making it a representative and challenging case for evaluating SIC prediction models [51]. Therefore, we compare the visualization results of our FH-Mamba with those of VMRNN and FCNet for the period from September 1 to 14, 2020, as shown in Fig. 5. The left columns show the predicted SIC maps for each model alongside the ground truth. The right columns highlight bias maps (predicted results minus ground truth). In the bias maps, positive errors are shown in red, and negative errors in blue. As can be observed, our FH-Mamba consistently shows smaller error regions compared to VMRNN and FCNet, particularly along the Arctic margin regions, where accurate prediction is more difficult due to complex dynamics. It is evident that the wavelet branch in FSSM improves the boundary detail prediction. In addition, our FH-Mamba better preserves fine spatial structures and boundary details, especially in the zoomed-in regions. This demonstrates the capability of the model to capture local textures and edges in sea ice prediction. Furthermore, across all three dates, FH-Mamba maintains consistent performance, whereas VMRNN and FCNet show fluctuating error patterns and more significant deviations from the ground truth. These results confirm that FH-Mamba delivers more accurate and stable SIC predictions with reduced biases and improved spatial detail reconstruction, particularly in Arctic marginal ice zones.

TABLE IV  
QUANTITATIVE EVALUATION OF SEA ICE EXTENT (SIE) ALIGNMENT  
USING IOU METRIC (2016.9–2020.9).

Time	VMRNN	FCNet	FH-Mamba (Ours)
2016.9	0.7665	0.8517	<b>0.8707</b>
2017.9	0.8769	0.9058	<b>0.9082</b>
2018.9	0.8788	0.9077	<b>0.9155</b>
2019.9	0.8601	0.9022	<b>0.9143</b>
2020.9	0.7970	0.8603	<b>0.8632</b>
<b>Average</b>	0.8359	0.8855	<b>0.8944</b>

**Sea Ice Extent Visualization and Evaluation.** To further quantify and visualize the model's ability at delineating the sea ice edge, which was qualitatively observed in the bias maps, we now evaluate its performance on the Sea Ice Extent (SIE) task. Fig. 6 compares the SIE of FH-Mamba, VMRNN, and FCNet, presenting the results for September 1st, 5th, 10th, and 14th from 2016 to 2020. SIE is defined as the area where the sea ice concentration is at least 15%, a standard threshold for distinguishing between open water and ice-covered regions. To quantitatively assess the model's ability to accurately classify these conditions, especially in the marginal ice zone, we introduce Intersection over Union (IoU) metrics. IoU specifically measures the structural alignment of the predicted ice extent against the ground truth. As detailed in Table IV, quantitative analysis for each test year from 2016 to 2020 reveals that FH-Mamba consistently achieves the highest IoU, with an average score of 0.8944, outperforming

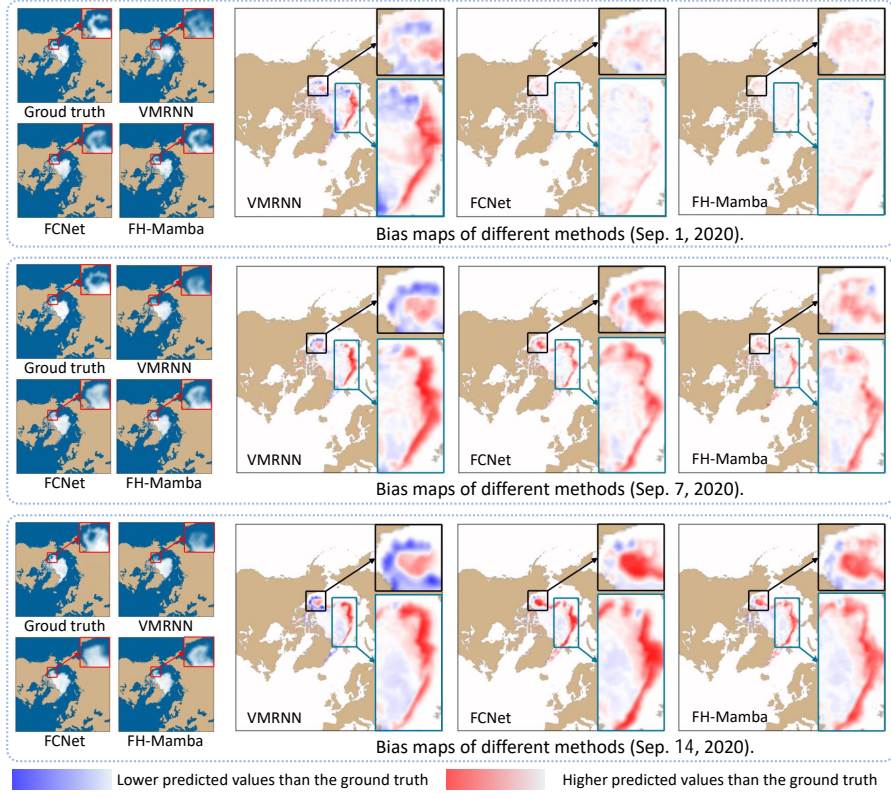


Fig. 5. The visualization results of VMRNN, FCNet, and our FH-Mamba during the period from September 1 to 14, 2020. The left columns show the predicted SIC maps for each model alongside the ground truth. The right columns highlight the bias maps (prediction minus ground truth). In the bias maps, positive errors are shown in red and negative errors in blue.

FCNet (0.8855) and VMRNN (0.8359). These metrics clarify the performance gap that is visually obscured by overlapping lines, demonstrating the performance of FH-Mamba in edge preservation and structural consistency.

**Analysis of Extreme Low-Ice Events.** To further evaluate FH-Mamba’s performance, we focused on three extreme climate events with the smallest sea ice extent values: September 2007, September 2012, and September 2020. The model was trained based on the following datasets: for 2007, SIC data from 1988-2006 was used, while for 2012, data from 1988-2011 was utilized. As for the 2020 analysis, we employed the model already described in the previous section. According to observational records, the lowest point of Arctic sea ice extent (3.387 million square kilometers) occurred on September 17, 2012, followed by records on September 16, 2020 (3.818 million square kilometers) and September 18, 2007 (4.14 million square kilometers). Fig. 7 displays the Arctic sea ice extent for specific September dates in three extreme years. The figure compares the prediction results of FH-Mamba, VMRNN and FCNet with the ground truth data. As indicated by the black rectangular box, FH-Mamba demonstrates higher prediction accuracy at the sea ice edge compared to other SOTA models, with its predictions being closely aligned with the ground truth (black line). This is attributed to FH-Mamba’s model design: it ensures the effectiveness of sequence and frequency feature fusion via the Hybrid Shuffle Attention (HSA) and achieves temporally consistent predictions by modeling the temporal dependencies of the input sequence. Consequently, this model

can more effectively learn the underlying spatiotemporal correlations in the data.

TABLE V  
PARAMETER, COMPUTATIONAL COMPLEXITY, INFERENCE TIME, AND TRAINING TIME COMPARISON OF DIFFERENT METHODS. THE **BOLD** AND UNDERLINE DENOTE THE BEST AND SECOND RESULTS.

Method	Params (M)	FLOPs (G)	Time (ms)	Training (s)
ConvLSTM	32.76	763.13	59.343	42,551.63
PredRNN	67.62	788.01	53.888	82,912.45
PredRNNv2	67.56	800.12	61.182	81,643.89
IceNet	34.54	291.05	48.500	26,450.33
SimVP	<b>14.83</b>	292.90	45.518	<b>6,826.91</b>
SwinLSTM	48.23	331.68	53.598	38,120.56
VMRNN	24.98	<u>240.43</u>	46.491	35,210.18
FCNet	56.66	532.63	57.200	<u>11,959.27</u>
IceMamba	44.15	300.66	<b>38.465</b>	23,501.15
<b>FH-Mamba (ours)</b>	<u>24.87</u>	<b>236.92</b>	<u>45.099</u>	17,797.63

#### E. Model Complexity and Inference Efficiency Comparison

Table V reports the comparison of model parameters, computational cost (FLOPs), training time, and inference time among different prediction methods. The proposed FH-Mamba achieves a trade-off between model size and efficiency. It contains 24.87M parameters and 236.92G FLOPs, which is the lowest computational cost among all methods. Moreover, FH-Mamba records the competitive inference speed of 45.099 ms, outperforming both convolutional–recurrent models (ConvLSTM, PredRNN, PredRNNv2, and IceNet) and Transformer-based methods (SwinLSTM). In terms of training overhead,

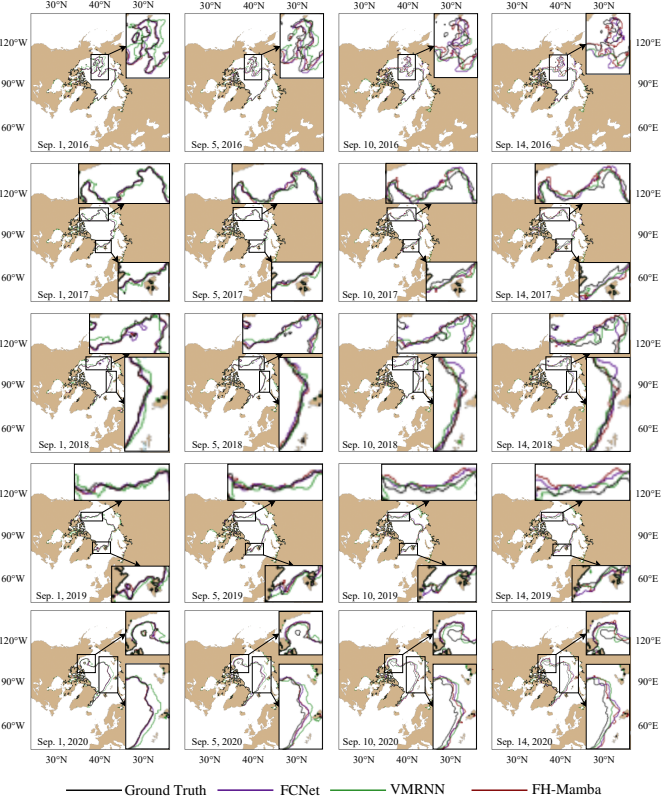


Fig. 6. Comparison of SIE on September 1st, 5th, 10th, and 14th of different years using various methods. The black line represents the SIE from the ground truth map. The green line signifies the SIE forecasted by the VMRNN. The purple line denotes the SIE predicted with the FCNet. And the red line represents the SIE predicted by our FH-Mamba.

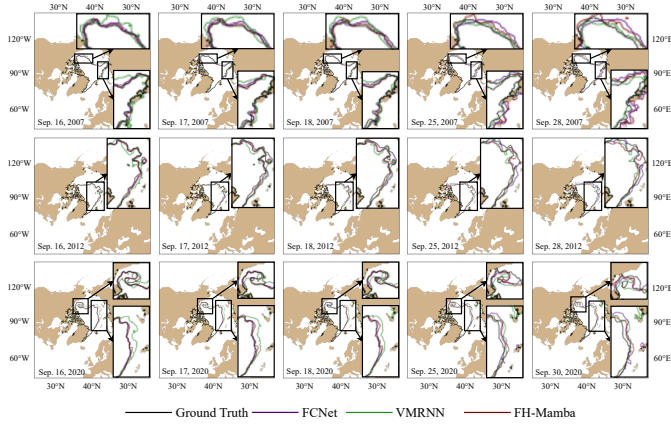


Fig. 7. Among the three extreme climate events with the smallest sea ice extent on record, the Arctic sea ice coverage reached its lowest points on the following dates: September 17, 2012, with an area of 3.39 million square kilometers; followed by September 16, 2020, with an area of 3.82 million square kilometers; and September 18, 2007, with an area of 4.14 million square kilometers.

FH-Mamba requires 17,797.63 s. It is worth noting that due to the early stopping mechanism, the total training time is influenced by convergence rates. Some models require more epochs to converge, resulting in longer training duration despite their single-step efficiency.

Although SimVP shows the smallest parameter count (14.83

M), its prediction accuracy is notably lower (as shown in subsequent tables). FH-Mamba, in contrast, achieves both high accuracy and high efficiency, demonstrating its effectiveness in capturing spatiotemporal dynamics while maintaining lightweight and real-time inference performance for Arctic sea-ice forecasting.

#### F. Ablation Studies

We first conducted comprehensive ablation studies to evaluate the contribution of each component in our FH-Mamba framework. Then, we analyze different scanning directions in 3D Hilbert and the impact of the HSA module.

**Effectiveness of Model Components.** The ablation study results shown in Table VI evaluate the effectiveness of three key components in the FH-Mamba framework: the 3D Hilbert Scanning Strategy (3DHSS), Wavelet transform, and the Hybrid Shuffle Attention (HSA) module. Using only 3DHSS yields better performance than using Wavelet or HSA alone, indicating that the 3D Hilbert scan mechanism is an integral component of our model. The model with all three components achieves the best overall performance with the lowest RMSE and MAE values. It confirms that each module contributes to performance gains and that their combination is complementary.

TABLE VI  
ABLATION STUDIES ON DIFFERENT MODULES.

3DHSS	Wavelet	HSA	RMSE (%) $\downarrow$	MAE (%) $\downarrow$
✓			8.109	2.831
	✓		6.748	2.117
		✓	6.795	2.279
✓	✓	✓	6.825	2.122
			<b>6.683</b>	<b>2.061</b>

While the numerical improvements from individual modules on the global RMSE metric may seem modest, this reflects a core challenge of the SIC prediction task. The vast majority of the Arctic region consists of stable thick ice or open water, where most models can achieve high accuracy. Consequently, global metrics are already high and tend to saturate. The true difficulty lies in the highly dynamic and complex marginal ice zones, which are the primary source of prediction errors. Our key components, such as the wavelet branch for high-frequency boundaries and 3DHSS for spatiotemporal locality, are specifically designed to address these challenging regions. Although these zones constitute a smaller portion of the total area, accurately forecasting their evolution is critical for practical applications like climate science and safe navigation. As visualized in Fig. 6, these modest numerical gains translate into significantly improved preservation of fine spatial structures and boundary details in these critical areas.

**Impact of 3D Scanning Directions.** Effective scanning is a key issue for Mamba when handling three-dimensional data. We compare five scanning directions on prediction performance in Table VII. We use the global scanning as in vanilla Mamba, Z-order scanning, Peano curve scanning, spatial-first Hilbert scanning, and temporal-first Hilbert scanning. The global scan in vanilla Mamba results in the worst performance,

with an RMSE of 7.041%, indicating its limited ability to preserve local spatio-temporal structures. In contrast, the Z-order scan achieves better results because it comprehensively considers both spatial and temporal correlations, even though it still suffers from dimensional discontinuities (fractures). The Peano curve further outperforms Z-order as it not only maintains spatio-temporal correlations but also eliminates these dimensional fractures. Ultimately, the Hilbert-based scanning routes achieve the best performance because they provide even stronger spatio-temporal locality than the Peano curve. Moreover, prioritizing temporal locality (temporal-first Hilbert) offers a slight advantage, suggesting that modeling temporal continuity first helps capture the dynamic evolution of sea ice more effectively.

TABLE VII  
ANALYSIS OF SCANNING DIRECTIONS. (INCLUDING ESTIMATED Z-ORDER AND PEANO)

Method	RMSE (%) ↓	MAE (%) ↓
Vanilla global scan	7.041	2.292
Z-order scan	6.915	2.210
Peano curve scan	6.755	2.107
Spatial-first Hilbert	6.689	2.068
Temporal-first Hilbert	<b>6.683</b>	<b>2.061</b>

**Effectiveness of the Feature Fusion Strategy.** Table VIII compares the performance of different fusion strategies for 3D Hilbert sequences and frequency features, including element-wise summation (termed Sum), channel-wise attention gating (termed CAGate), and our HSA. CAGate and HSA perform better than Sum, indicating that attention-based models better capture the interactions between sequence and frequency features. Our HSA achieves the best performance in terms of both RMSE and MAE. It effectively captures the complementary information between sequence and frequency features, leading to more accurate Arctic SIC predictions.

TABLE VIII  
PERFORMANCE COMPARISON OF FEATURE FUSION.

Method	RMSE (%) ↓	MAE (%) ↓
Sum	7.017	2.151
CAGate	6.775	2.120
HSA (ours)	<b>6.683</b>	<b>2.061</b>

**Justification for the Wavelet Transform Branch.** A key challenge in SIC prediction is capturing the fine-grained details of marginal ice zones, which correspond to high-frequency information in the spatial domain. To validate that our choice of a Discrete Wavelet Transform (DWT) branch is effective for this purpose, we conducted a comparative analysis against several alternative designs: 1) a baseline model without any specialized frequency branch, 2) a branch using simple Multi-Scale Convolutions (MSC) with different kernel sizes to capture features at various scales, and 3) a STFT-based Spectral Attention (STFT-SA) module that operates in the Fourier domain. As shown in Table IX, while both MSC and STFT-SA offer improvements over the baseline, our DWT-based approach achieves the lowest error. This suggests that

the multi-resolution analysis capability of DWT is particularly effective at decomposing and emphasizing the precise boundary details critical for SIC forecasting, justifying its selection over other frequency and multi-scale analysis techniques.

TABLE IX  
PERFORMANCE COMPARISON OF DIFFERENT HIGH-FREQUENCY FEATURE EXTRACTION BRANCHES. OUR DWT-BASED APPROACH YIELDS THE BEST RESULTS.

Method	RMSE (%) ↓	MAE (%) ↓
None (Baseline)	6.713	2.092
MSC (Multi-scale Conv)	6.701	2.084
STFT-SA	6.692	2.072
DWT (Ours)	<b>6.683</b>	<b>2.061</b>

**Impact of Different Wavelet Bases.** To justify our choice of the wavelet basis function in the FSSM, we conducted a comparative analysis using three different wavelet families: Haar, Daubechies (db2), and Biorthogonal (bior1.3). The Haar wavelet is known for its capability to capture sudden transitions, making it suitable for detecting sea ice edges. Daubechies and Biorthogonal wavelets offer higher vanishing moments and different symmetry properties.

TABLE X  
PERFORMANCE COMPARISON OF DIFFERENT WAVELET BASES.

Wavelet Basis	RMSE (%)	MAE (%)
Daubechies (db2)	6.691	2.068
Biorthogonal (bior1.3)	6.689	2.065
Haar (Ours)	<b>6.683</b>	<b>2.061</b>

As shown in Table X, the performance differences among these bases are negligible. The RMSE fluctuates within a narrow range of 0.01%, and MAE within 0.007%. This suggests that the proposed FH-Mamba is robust to the selection of wavelet bases. We adopted the Haar wavelet in our final model primarily due to its computational simplicity and effectiveness in preserving high-frequency boundary information without introducing additional computational overhead.

#### G. Parameter Sensitivity Analysis

**Impact of the Number of FSSM Blocks.** The number of Frequency-enhanced State Space Modules (FSSMs) is an important parameter that may affect the performance of Arctic Sea Ice Concentration (SIC) prediction. In this study, we have conducted extensive experiments to study FSSM, and the results are shown in Fig. 8(a). As the number of FSSM modules increases from 1 to 5, the RMSE consistently decreases. This trend indicates that incorporating more FSSM modules improves prediction accuracy. However, we observe a clear law of diminishing returns beyond three modules. The incremental accuracy gain from 3 to 5 modules is negligible compared to the increase in computational complexity. In light of this efficiency-accuracy trade-off, we deliberately select 3 modules as the optimal configuration. This choice ensures the model retains its prediction capabilities while remaining sufficiently lightweight for the rapid processing requirements of large-scale Arctic spatiotemporal data.

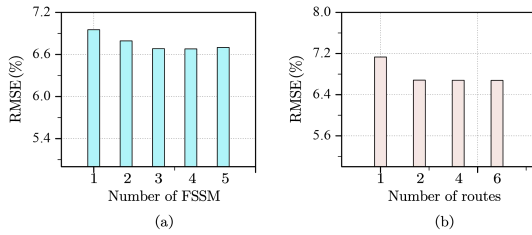


Fig. 8. Parameter analysis. (a) Relationship between the number of FSSM modules and the corresponding RMSE. (b) Relationship between the number of routes in 3D Hilbert scanning and the corresponding RMSE.

**Impact of the Number of 3D Hilbert Scan Routes.** The 3D Hilbert scan can have multiple valid paths, depending on the configuration and transformation rules used during construction. In practice, after generating the 3D Hilbert curve, we can obtain two scanning paths: a forward scan and a backward scan. Next, by rotating the input 3D data, we can obtain more scanning routes. In Fig. 8(b), the bar chart shows the effect of varying the number of 3D Hilbert scanning routes on RMSE for prediction performance. When we use two routes, the RMSE significantly decreases compared with using only 1 route. However, when the number of routes increases beyond 2, the RMSE remains nearly unchanged. Therefore, in our implementations, we use 2 routes for 3D Hilbert scanning.

**Long-Term Iterative Forecasting.** To predict longer SIC sequences, we explore the performance of FH-Mamba for recursive prediction. Specifically, the predicted results for the first 14 days are used as the inputs of FH-Mamba to predict the SIC for the next 14 days. Likewise, the predicted SIC for the next 14 days can be used as inputs to generate a 42-day SIC prediction. The experimental results for recursive prediction are shown in Table XI. It can be observed that when the number of recursive steps increases (extending the prediction horizon to 28, 42, and 56 days), the prediction performance gradually degrades. This performance decline is expected due to the accumulation of prediction errors as the model repeatedly uses its own outputs as inputs for subsequent predictions. Despite this, for 56-day SIC prediction, the MAE increases to 3.697%, revealing limitations for precise navigation due to recursive error accumulation. While the model captures the general evolution, its reliability for real-world applications decreases at longer horizons.

TABLE XI  
PERFORMANCE OF OUR FH-MAMBA WITH DIFFERENT Recursive STEPS.

Recursive step	Prediction period	RMSE $\downarrow$	MAE $\downarrow$	NSE $\uparrow$
0	14 days	<b>6.683</b>	<b>2.061</b>	<b>96.609</b>
1	28 days	9.616	3.064	87.569
2	42 days	11.462	3.690	81.177
3	56 days	11.634	3.697	81.166

#### H. Uncertainty Quantification

While our proposed FH-Mamba is designed as a deterministic model providing point forecasts, real-world applications

such as ensuring safe navigation often benefit from understanding the model's prediction uncertainty. To this end, we extend our framework to enable probabilistic forecasting, allowing it to quantify the uncertainty associated with its predictions.

This extension is achieved by modifying the model's output layer. Instead of predicting a single value for each grid point, the probabilistic version is trained to predict the parameters of a Gaussian distribution: the mean  $\mu$  and the standard deviation  $\sigma$ . The predicted mean  $\mu$  represents the most likely SIC value, analogous to the output of our deterministic model. The standard deviation  $\sigma$  represents the model's uncertainty; a larger  $\sigma$  indicates lower confidence in the prediction for that specific point. To ensure that  $\sigma$  is always positive, the network's raw output for the standard deviation is passed through a softplus activation function. For training this probabilistic model, we replace the L1 loss with the Negative Log-Likelihood (NLL) loss, which is a standard objective for learning probability distributions. The goal is to maximize the likelihood of the ground truth data given the predicted distribution.

The experimental results are presented in Table XII. As can be seen, the probabilistic version of FH-Mamba experiences a negligible increase in RMSE and MAE compared to its deterministic counterpart. This demonstrates that the model can provide valuable uncertainty information without significantly compromising its point prediction accuracy, enhancing its practical utility for critical decision-making processes.

TABLE XII  
PERFORMANCE COMPARISON BETWEEN THE DETERMINISTIC AND PROBABILISTIC VERSIONS OF FH-MAMBA.

Model Version	RMSE (%) $\downarrow$	MAE (%) $\downarrow$	NLL $\downarrow$
Deterministic	6.683	2.061	N/A
Probabilistic	6.712	2.075	-2.453

## V. CONCLUSION

In this paper, we propose FH-Mamba, a novel framework for short-term Arctic SIC prediction. We focus on two challenges:

For the first challenge: **How can we effectively model temporal correlations by using SSMs?** To address this, we employ 3D Hilbert scanning mechanism that enhances the model's ability to learn spatiotemporal patterns. Unlike conventional global scans, the scanning in our FH-Mamba is performed across both temporal and spatial dimensions simultaneously. It enables the model to better capture local temporal correlations and subtle transitions in sea ice evolution. Experimental comparisons with SOTA methods demonstrate that our FH-Mamba effectively improves the Arctic SIC prediction. The model's performance improvements were consistently demonstrated on both the OSI-450a1 and AMSR2 datasets.

For the second challenge: **How can we enhance the details of the Arctic margin regions?** To tackle this, we employ wavelet transform to amplify the high-frequency components. Additionally, we design a HSA module to further exploit the complementary information between sequence features and frequency features. HSA performs channel-wise attention to adaptively fuse these features, allowing the model to better

capture complex dependencies across both domains. Visualization results of predicted SIC maps clearly show that FH-Mamba produces sharper and more accurate boundary details, particularly in marginal ice zones.

Overall, FH-Mamba provides a method for fine-grained and high-fidelity Arctic SIC forecasting, offering valuable insights for future developments in physics-aware and frequency-enhanced SSM-based ocean prediction models.

## REFERENCES

- [1] C. L. Parkinson and N. E. DiGirolamo, "Sea ice extents continue to set new records: Arctic, antarctic, and global results," *Remote Sensing of Environment*, vol. 267, p. 112753, 2021.
- [2] P. Tepes, N. Gourmelen, P. Nienow, M. Tsamados, A. Shepherd, and F. Weissgerber, "Changes in elevation and mass of arctic glaciers and ice caps, 2010–2017," *Remote Sensing of Environment*, vol. 261, p. 112481, 2021.
- [3] Q. Yang, L. Mu, X. Wu, J. Liu, F. Zheng, J. Zhang, and C. Li, "Improving arctic sea ice seasonal outlook by ensemble prediction using an ice-ocean model," *Atmospheric research*, vol. 227, pp. 14–23, 2019.
- [4] S. Horvath, J. Stroeve, B. Rajagopalan, and W. Kleiber, "A bayesian logistic regression for probabilistic forecasts of the minimum september arctic sea ice cover," *Earth and Space Science*, vol. 7, no. 10, pp. 1–18, 2020.
- [5] V. Guemas, E. Blanchard-Wrigglesworth, M. Chevallier, J. J. Day, M. Déqué, F. J. Doblas-Reyes, N. S. Fučkar, A. Germe, E. Hawkins, S. Keeley *et al.*, "A review on arctic sea-ice predictability and prediction on seasonal to decadal time-scales," *Quarterly Journal of the Royal Meteorological Society*, vol. 142, no. 695, pp. 546–561, 2016.
- [6] V. Capone, A. Casolari, and F. Camastrà, "Spatio-temporal prediction using graph neural networks: A survey," *Neurocomputing*, vol. 643, p. 130400, 2025.
- [7] S. Wang, J. Cao, and P. S. Yu, "Deep learning for spatio-temporal data mining: A survey," *IEEE Transactions on Knowledge and Data Engineering*, vol. 34, no. 8, pp. 3681–3700, 2022.
- [8] T. R. Andersson, J. S. Hosking, M. Pérez-Ortiz, B. Paige, A. Elliott, C. Russell, S. Law, D. C. Jones, J. Wilkinson, T. Phillips, J. Byrne, S. Tietsche, B. B. Sarojini, E. Blanchard-Wrigglesworth, Y. Aksенov, R. Downie, and E. Shuckburgh, "Seasonal arctic sea ice forecasting with probabilistic deep learning," *Nature Communications*, vol. 12, no. 1, pp. 1–12, 2021.
- [9] Y. Ren, X. Li, and W. Zhang, "A data-driven deep learning model for weekly sea ice concentration prediction of the pan-arctic during the melting season," *IEEE Transactions on Geoscience and Remote Sensing*, vol. 60, pp. 1–19, 2022.
- [10] J. Zhang, F. Gao, Y. Gan, J. Dong, and Q. Du, "Frequency-compensated network for daily arctic sea ice concentration prediction," *IEEE Transactions on Geoscience and Remote Sensing*, vol. 63, pp. 1–15, 2025.
- [11] J. Xu, S. Tu, W. Yang, B. Fei, S. Li, K. Liu, Y. Luo, L. Ma, and L. Bai, "Icediff: High resolution and high-quality arctic sea ice forecasting with generative diffusion prior," in *Proceedings of the Computer Vision and Pattern Recognition Conference (CVPR)*, June 2025, pp. 10567–10576.
- [12] A. Vaswani, N. Shazeer, N. Parmar, J. Uszkoreit, L. Jones, A. N. Gomez, L. u. Kaiser, and I. Polosukhin, "Attention is all you need," in *Proceedings of Advances in Neural Information Processing Systems (NeurIPS)*, vol. 30, 2017, pp. 1–13.
- [13] H. Zhang, C. Chen, L. Mei, Q. Liu, and J. Mao, "Mamba retriever: Utilizing mamba for effective and efficient dense retrieval," in *Proceedings of the 33rd ACM International Conference on Information and Knowledge Management (CIKM)*, 2024, p. 4268–4272.
- [14] S. Zhou, H. Zeng, Y. Lu, T. Shao, K. Tang, Y. Chen, J. Liu, and J. Su, "Binarized mamba-transformer for lightweight quad bayer hybridevs demosaicing," in *Proceedings of the Computer Vision and Pattern Recognition Conference (CVPR)*, June 2025, pp. 8817–8827.
- [15] B. Li, H. Zhao, W. Wang, P. Hu, Y. Gou, and X. Peng, "Mair: A locality- and continuity-preserving mamba for image restoration," in *Proceedings of the Computer Vision and Pattern Recognition Conference (CVPR)*, June 2025, pp. 7491–7501.
- [16] Z. Zhang, Z. Hu, B. Cao, P. Li, Q. Su, Z. Dong, and T. Wang, "Wiener filter-based mamba for remote sensing image super-resolution with novel degradation," *IEEE Journal of Selected Topics in Applied Earth Observations and Remote Sensing*, vol. 18, pp. 26295–26308, 2025.
- [17] Y. Xu, C. Han, S. Chen, Y. Jin, Y. Miao, H. Guo, and D. Wang, "Phdmamba: Progressive hybrid mamba for hyperspectral image classification," *IEEE Geoscience and Remote Sensing Letters*, vol. 22, pp. 1–5, 2025.
- [18] L. Li and B. Wang, "Dpmn: Deep prior mamba network for hyperspectral anomaly detection," *IEEE Transactions on Geoscience and Remote Sensing*, vol. 63, pp. 1–16, 2025.
- [19] L. Liang, J. Zhang, P. Duan, X. Kang, T. Xinzhang Wu, J. Li, and A. Plaza, "Lkma: Learnable kernel and mamba with spatial-spectral attention fusion for hyperspectral image classification," *IEEE Transactions on Geoscience and Remote Sensing*, vol. 63, pp. 1–14, 2025.
- [20] A. Gu and T. Dao, "Mamba: Linear-time sequence modeling with selective state spaces," in *Proceedings of the Conference on Language Modeling (COLM)*, 2024, pp. 1–23.
- [21] J. Chi and H.-C. Kim, "Prediction of arctic sea ice concentration using a fully data driven deep neural network," *Remote Sensing*, vol. 9, no. 12, pp. 1–22, 2017.
- [22] Y. J. Kim, H.-C. Kim, D. Han, S. Lee, and J. Im, "Prediction of monthly arctic sea ice concentrations using satellite and reanalysis data based on convolutional neural networks," *The Cryosphere*, vol. 14, no. 3, pp. 1083–1104, 2020.
- [23] Y. Ren, X. Li, and Y. Wang, "Sinet v1.0: a transformer-based deep learning model for seasonal arctic sea ice prediction by incorporating sea ice thickness data," *Geoscientific Model Development*, vol. 18, no. 9, pp. 2665–2678, 2025.
- [24] O. Ronneberger, P. Fischer, and T. Brox, "U-Net: Convolutional networks for biomedical image segmentation," in *Proceedings of Medical Image Computing and Computer-Assisted Intervention (MICCAI)*, 2015, pp. 234–241.
- [25] Z. Liu, Y. Lin, Y. Cao, H. Hu, Y. Wei, Z. Zhang, S. Lin, and B. Guo, "Swin transformer: Hierarchical vision transformer using shifted windows," in *2021 IEEE/CVF International Conference on Computer Vision (ICCV)*, 2021, pp. 9992–10002.
- [26] W. Wang, W. Yang, L. Wang, G. Wang, and R. Lei, "Seasonal forecasting of pan-arctic sea ice with state space model," *npj Climate and Atmospheric Science*, vol. 8, no. 1, p. 172, May 2025.
- [27] L. Liu, M. Zhang, J. Yin, T. Liu, W. Ji, Y. Piao, and H. Lu, "Defmamba: Deformable visual state space model," in *Proceedings of the Computer Vision and Pattern Recognition Conference (CVPR)*, June 2025, pp. 8838–8847.
- [28] A. Shaker, S. T. Wasim, S. Khan, J. Gall, and F. S. Khan, "Groupmamba: Efficient group-based visual state space model," in *Proceedings of the Computer Vision and Pattern Recognition Conference (CVPR)*, June 2025, pp. 14912–14922.
- [29] A. Hatamizadeh and J. Kautz, "Mambavision: A hybrid mamba-transformer vision backbone," in *Proceedings of the Computer Vision and Pattern Recognition Conference (CVPR)*, June 2025, pp. 25261–25270.
- [30] S. Lee, J. Choi, and H. J. Kim, "Efficientvimb: Efficient vision mamba with hidden state mixer based state space duality," in *Proceedings of the Computer Vision and Pattern Recognition Conference (CVPR)*, June 2025, pp. 14923–14933.
- [31] H. Wu, Y. Yang, H. Xu, W. Wang, J. Zhou, and L. Zhu, "Rainmamba: Enhanced locality learning with state space models for video deraining," in *ACM Multimedia*, 2024, p. 7881–7890.
- [32] H.-L. Chen and Y.-I. Chang, "All-nearest-neighbors finding based on the hilbert curve," *Expert Systems with Applications*, vol. 38, no. 6, pp. 7462–7475, 2011.
- [33] D. Hilbert, "Ueber die stetige abbildung einer linie auf ein flächenstück," *Mathematische Annalen*, vol. 38, no. 3, pp. 459–460, 1891.
- [34] A. Keller, C. Wächter, and N. Binder, "Rendering along the hilbert curve," *arXiv: 2207.05415*, pp. 1–13, 2022.
- [35] R. Uddin, C. V. Ravishankar, and V. J. Tsotras, "Indexing moving object trajectories with hilbert curves," 2018, p. 416–419.
- [36] D. Liang, X. Zhou, W. Xu, X. Zhu, Z. Zou, X. Ye, X. Tan, and X. Bai, "Pointmamba: A simple state space model for point cloud analysis," in *Advances in Neural Information Processing Systems (NeurIPS)*, 2024.
- [37] B. Moon, H. Jagadish, C. Faloutsos, and J. Saltz, "Analysis of the clustering properties of the hilbert space-filling curve," *IEEE Transactions on Knowledge and Data Engineering*, vol. 13, no. 1, pp. 124–141, 2001.
- [38] A. Butz, "Alternative algorithm for hilbert's space-filling curve," *IEEE Transactions on Computers*, vol. C-20, no. 4, pp. 424–426, 1971.
- [39] J. Chen, L. Yu, and W. Wang, "Hilbert space filling curve based scanner for point cloud attribute compression," *IEEE Transactions on Image Processing*, vol. 31, pp. 4609–4621, 2022.

- [40] J. Weissenböck, B. Fröhler, E. Gröller, J. Kastner, and C. Heinzl, “Dynamic volume lines: Visual comparison of 3d volumes through space-filling curves,” *IEEE Transactions on Visualization and Computer Graphics*, vol. 25, no. 1, pp. 1040–1049, 2019.
- [41] L. Zhu, B. Liao, Q. Zhang, X. Wang, W. Liu, and X. Wang, “Vision mamba: Efficient visual representation learning with bidirectional state space model,” in *Proceedings of International Conference on Machine Learning (ICML)*, 2024, pp. 1–13.
- [42] T. Lavergne, A. M. Sørensen, S. Kern, R. Tonboe, D. Notz, S. Aaboe, L. Bell, G. Dybkjær, S. Eastwood, C. Gabarro *et al.*, “Version 2 of the eumetsat osi saf and esa cci sea-ice concentration climate data records,” *The Cryosphere*, vol. 13, no. 1, pp. 49–78, 2019.
- [43] D. P. Dee, S. M. Uppala, A. J. Simmons, P. Berrisford, P. Poli, S. Kobayashi, U. Andrae, M. Balmaseda, G. Balsamo, d. P. Bauer *et al.*, “The era-interim reanalysis: Configuration and performance of the data assimilation system,” *Journal of the Royal Meteorological Society*, vol. 137, no. 656, pp. 553–597, 2011.
- [44] H. Hung, R. Kallenborn, K. Breivik, Y. Su, E. Brorström-Lundén, K. Olafsdottir, J. M. Thorlacius, S. Leppänen, R. Bossi, H. Skov *et al.*, “Atmospheric monitoring of organic pollutants in the arctic under the arctic monitoring and assessment programme (amap): 1993–2006,” *Science of the Total Environment*, vol. 408, no. 15, pp. 2854–2873, 2010.
- [45] G. Spreen, L. Kaleschke, and G. C. Heygster, “Sea ice remote sensing using amsr-e 89-ghz channels,” *Journal of Geophysical Research*, vol. 113, 2008.
- [46] Y. Wang, M. Long, J. Wang, Z. Gao, and P. S. Yu, “Predrnn: Recurrent neural networks for predictive learning using spatiotemporal lstms,” in *Advances in Neural Information Processing Systems (NeurIPS)*, I. Guyon, U. V. Luxburg, S. Bengio, H. Wallach, R. Fergus, S. Vishwanathan, and R. Garnett, Eds., vol. 30, 2017, pp. 1–13.
- [47] Y. Wang, H. Wu, J. Zhang, Z. Gao, J. Wang, S. Y. Philip, and M. Long, “Predrnn: A recurrent neural network for spatiotemporal predictive learning,” *IEEE Transactions on Pattern Analysis and Machine Intelligence*, vol. 45, no. 2, pp. 2208–2225, 2022.
- [48] Z. Gao, C. Tan, L. Wu, and S. Z. Li, “Simvp: Simpler yet better video prediction,” in *IEEE/CVF Conference on Computer Vision and Pattern Recognition (CVPR)*, 2022, pp. 3170–3180.
- [49] S. Tang, C. Li, P. Zhang, and R. Tang, “Swinlstm: Improving spatiotemporal prediction accuracy using swin transformer and lstm,” in *2023 IEEE/CVF International Conference on Computer Vision (ICCV)*, 2023, pp. 13 424–13 433.
- [50] Y. Tang, P. Dong, Z. Tang, X. Chu, and J. Liang, “Vmrrnn: Integrating vision mamba and lstm for efficient and accurate spatiotemporal forecasting,” in *2024 IEEE/CVF Conference on Computer Vision and Pattern Recognition Workshops (CVPRW)*, 2024, pp. 5663–5673.
- [51] J. Stroeve and D. Notz, “Changing state of arctic sea ice across all seasons,” *Environmental Research Letters*, vol. 13, no. 10, p. 103001, 2018.